SCIENTIFIC Publishing Limited

**Neurolinguistic Communication Intervention**

https://ojs.ukscip.com/index.php/nci

*Article*

# Network Signatures of Verbal Ability in Autism: A Multisite fMRI Study Using Graph Theory and Machine Learning

**Huibin Ma [1], Jinying Wu [1], Lanfen Chen [2], Jiaying Song [1], Hang Zhang [2], Zeqi Hao [3], Linlin Zhan [4], Lulu Cheng [5,*] and Xize Jia [3,6,*]**

[1] School of Information and Electronics Technology, Jiamusi University, Jiamusi 154007, China

[2] School of Medical Imaging, Shandong Second Medical University, Weifang 261053, China

[3] School of Psychology, Zhejiang Normal University, Jinhua 321004, China

[4] Faculty of Western Languages, Heilongjiang University, Harbin 150080, China

[5] School of Foreign Studies, China University of Petroleum (East China), Qingdao 266580, China

[6] Intelligent Laboratory of Zhejiang Province in Mental Health and Crisis Intervention for Children and Adolescents, Zhejiang Normal University, Jinhua 321004, China

[*] Correspondence: cllsgnh@163.com (L.C.); jiaxize@foxmail.com (X.J.)

**Received:** 3 August 2025; **Revised:** 15 October 2025; **Accepted:** 17 December 2025; **Published:** 2 January 2026

**Abstract:** Autism spectrum disorder (ASD) is associated with atypical functional connectivity (FC), but its relationship with verbal ability remains unclear. In this study, resting-state functional magnetic resonance imaging (rs-fMRI) data from 219 individuals with ASD and 322 healthy controls (HCs) with valid verbal intelligence quotient (VIQ) scores were obtained from 12 sites in the Autism Brain Imaging Data Exchange (ABIDE) database. Region of interest (ROI)-based FC and whole-brain network metrics were computed and correlated with VIQ. Three feature sets—raw connectivity and topology, group-difference metrics, and group-difference metrics combined with VIQ—were evaluated using support vector machine (SVM) and manifold learning. ASD showed widespread FC alterations with overall increases and localized decreases in specific networks. At the global level, ASD patients exhibited a significantly lower area under the receiver operating characteristic curve (AUC) specifically for the normalized clustering coefficient γ compared with HCs. Nodal analyses revealed increased degree centrality and efficiency in subcortical and frontal regions, but decreased values in limbic and temporal regions in ASD. Centrality of the anterior cingulate cortex showed a negative correlation with VIQ, while nodal efficiency and degree centrality in occipital regions showed positive correlations. Classification using the raw feature set achieved the best overall performance under the Principal Component Analysis-Uniform Manifold Approximation and Projection-Support Vector Machine (PCA-UMAP-SVM) pipeline, whereas group-difference features augmented with VIQ yielded the highest AUC among the standard SVM models. These results suggest that VIQ-anchored network features may help explain variability in verbal ability and brain organization in ASD.

**Keywords:** Autism Spectrum Disorder; Functional Connectivity; Manifold Learning; Machine Learning; Graph Theoretical Analysis; Verbal Ability

## 1. Introduction

Autism spectrum disorder (ASD) is a neurodevelopmental condition characterized by impairments in social communication, the presence of restricted interests, and repetitive or stereotyped behaviors [1]. Language impairment is a prominent feature of ASD, often reflected in reduced overall verbal abilities and difficulties in efficiently processing and integrating linguistic information during comprehension [2]. Despite the documented impact of language impairments, the neural mechanisms underlying verbal ability and its relationship with verbal intelligence quotient (VIQ) in ASD remain unclear.

Recently, resting-state functional magnetic resonance imaging (rs-fMRI), with its high temporal and spatial resolution and non-invasive nature [3,4], has become a pivotal tool for probing the neural mechanisms of ASD [5]. Functional Connectivity (FC) analysis and graph theory have been widely used to study the neural substrates of verbal ability in ASD [6–8], and altered network organization has been repeatedly reported as a defining feature of the disorder [9,10]. FC analysis assesses the temporal synchrony of neural activity between pairs of brain regions, whereas graph-theoretical analysis applies mathematical frameworks to represent the brain as a network of nodes (brain regions) and edges (FC), enabling the characterization of network topology through small-world properties, global metrics, and nodal metrics [11–13]. Prior studies have reported language-related network differences in ASD, with Lee et al. [6] reporting atypical degree centrality (DC) within frontal and temporal language regions in ASD adults. However, most previous work has relied on social communication measures, such as the autism diagnostic observation schedule (ADOS), to interpret network alterations, with relatively few studies directly assessing verbal ability [6,14]. Notably, as a standardized index of verbal cognitive ability, VIQ has been identified as a critical predictor of ASD symptom severity and long-term functional outcomes [15]. Therefore, employing VIQ as a direct behavioral index may provide deeper insights into the specific neural correlates of linguistic heterogeneity in ASD.

Additionally, machine learning (ML) has become an essential tool for the diagnosis and prediction of neurological disorders [16,17]. Distinct from traditional inferential statistics, ML can integrate information across multiple voxels or regions by identifying multivariate patterns rather than focusing on isolated features, which helps reduce misdiagnosis rates in clinical practice [18]. Support vector machine (SVM) is a class of supervised algorithms designed to find the optimal separating hyperplane for classification tasks [19]. Using features derived from FC and graph-theoretical network metrics, the SVM has been extensively used for classifying various neurological conditions in ASD [20–22]. However, SVM performance can be compromised by the high dimensionality, noise, and redundancy of neuroimaging-derived features [23], necessitating appropriate feature selection or dimensionality reduction to ensure robust classification. Principal component analysis (PCA) decomposes fMRI time series into orthogonal components, allowing low-variance (noise) components to be removed and thereby enhancing blood-oxygen-level-dependent (BOLD) contrast sensitivity [24]. Nevertheless, as a linear method, PCA may not fully capture the nonlinear structure inherent in high-dimensional neuroimaging data. To address this limitation, uniform manifold approximation and projection (UMAP) is a nonlinear manifold-learning technique that projects high-dimensional data into a low-dimensional embedding by jointly optimizing local neighborhood preservation and global topological structure [25,26]. In rs-fMRI, UMAP has been applied to FC matrices and voxel-wise connectivity profiles to reveal intrinsic network organization and to distinguish among cognitive or clinical states. Accordingly, we propose two distinct pipelines for identifying FC neuromarkers in ASD to evaluate their diagnostic utility: one using manual feature selection for dimensionality reduction followed by SVM classification, and another that performs automated dimensionality reduction through PCA combined with UMAP embedding prior to SVM classification. Furthermore, to ensure a robust and threshold-independent evaluation of diagnostic utility in such high-dimensional spaces, we emphasize the area under the receiver operating characteristic curve (AUC) as the primary performance metric. Compared to simple accuracy, AUC provides a more comprehensive reflection of a classifier's discriminative power [27,28], especially when dealing with the clinical heterogeneity inherent in multisite datasets [29–31].

In the present study, given that most previous investigations have been constrained by relatively small sample sizes, limiting generalizability [32–34], we leveraged the open-access Autism Brain Imaging Data Exchange (ABIDE; http://fcon_1000.projects.nitrc.org/indi/abide/) repository to address the sample size limitations and to enable assessment of reproducibility across multiple sites [35]. We examine multisite neuroimaging data, conduct correlation analyses, and assess the classification performance of three feature sets: raw connectivity, group-difference

connectivity and network metrics, and a VIQ-augmented differential-language set. We then test three hypotheses: (1) individuals with ASD would show altered whole-brain FC and network topology relative to healthy controls (HCs); (2) these alterations, particularly in language- and executive control-related networks, would be associated with VIQ; and (3) a feature-engineering strategy incorporating VIQ, combined with PCA-UMAP dimensionality reduction, would improve the classification performance of SVM models relative to manual feature selection.

## 2. Materials and Methods

### 2.1. Participants

We used neuroimaging data from the ABIDE initiative, including ABIDE I (http://fcon_1000.projects.nitrc.org/indi/abide/abide_I.html) [35] and ABIDE II (http://fcon_1000.projects.nitrc.org/indi/abide/abide_II.html) [36]. The inclusion criteria were as follows: (1) availability of both functional and structural MRI data; (2) successful spatial normalization; (3) head motion ≤ 3 mm in translation and ≤ 3° in rotation; (4) inclusion of both ASD and HCs within each site; and (5) right-handedness to control for lateralization effects. After applying these criteria, we further included participants with available and valid VIQ scores, as assessed by the Wechsler Abbreviated Scale of Intelligence (WASI) [37]. This yielded a final sample of 541 participants, including 219 individuals with ASD and 322 HCs.

Additional information on scanning protocols, ethical approvals, and data acquisition procedures can be found on the ABIDE project website (http://fcon_1000.projects.nitrc.org/indi/abide/).

### 2.2. Rs-fMRI Data Preprocessing

All of the functional images were preprocessed using the rs-fMRI Data Analysis Toolkit plus (RESTplus V1.28; http://restfmri.net/forum/restplus) [38] in MATLAB 2022b (MathWorks, Natick, MA, USA). Specifically, the following steps were conducted: (1) discarding the first 10 time points; (2) slice timing correction; (3) head motion correction; (4) spatial normalization to the Montreal Neurological Institute (MNI) space using deformation fields derived from the new segmentation of structural images, followed by resampling to $3 \times 3 \times 3$ $mm^3$; (5) spatial smoothing with a 4 mm full width at half maximum (FWHM); (6) linear detrending; (7) nuisance signal regression with the Friston-24 head motion parameters as covariates [39]; (8) bandpass filtering in conventional (0.01–0.08 Hz) bands.

### 2.3. FC Analysis

To construct subject-specific FC matrices, we employed the Automated Anatomical Labeling (AAL90) atlas to define the brain network architecture. This atlas partitions the brain into 90 anatomically constrained regions of interest (ROIs) and is widely recognized for its utility in identifying biomarkers for various neuropsychiatric disorders [40–43].

To facilitate the functional interpretation of whole-brain FC alterations, each of the 90 AAL regions was assigned—via its MNI centroid—to one of the seven intrinsic functional networks defined by Yeo et al. [44]. These networks include the visual (VN), somatomotor (SMN), dorsal attention (DAN), ventral attention (VAN), frontoparietal (FPN), limbic, and default-mode (DMN) networks. This mapping aligns anatomical regions with established functional hierarchies and topographically specific connectivity patterns [44,45].

For each subject, blood-oxygen-level-dependent (BOLD) signals were extracted from each ROI. FC was quantified as the Pearson correlation coefficient between the time series of each ROI pair. The Pearson correlation coefficients were normalized using Fisher-Z transformation. The resulting FC matrix was symmetric, with each element representing the strength of temporal coherence between two ROIs.

### 2.4. Network Metrics

To characterize the global topology and regional attributes of brain functional networks across different sparsity thresholds, we constructed weighted networks over a cost range from 0.05 to 0.50 in 0.05 increments and computed both global metrics and nodal metrics using the GRETNA (v2.0.0) software package [46,47].

The global metrics include (1) small-world properties—average clustering coefficient (Cp), characteristic path length (Lp), global clustering coefficient (γ), normalized characteristic path length (λ), and small-worldness (σ)—

and (2) network efficiency measures—global efficiency (Eglob) and Eloc. The normalized metrics were derived as γ = Cp/Cprand and λ = Lp/Lprand, where Cprand and Lprand are the average values computed from 100 matched random networks. These normalized indices quantify the topological shift of the functional brain network relative to a random configuration. High Cp, γ, and Eloc indicate strong functional segregation, reflecting local interconnectivity within the network. Conversely, low Lp, λ, and high Eglob suggest efficient functional integration, facilitating global information exchange. Small-worldness quantifies the balance between local specialization and global communication, with small-world networks exhibiting both high global clustering coefficients (γ > 1) characteristic of regular lattices and short characteristic path lengths (λ ≈ 1) typical of random networks [48].

To assess regional node properties, we calculated betweenness centrality (BC), degree centrality (DC), nodal efficiency (NE), and nodal local efficiency (NLE). BC quantifies a node's influence on information flow, with higher values indicating a greater role in communication pathways [49]. DC measures the number of direct connections a node has, reflecting its connectivity [46]. NE evaluates a node's capacity for parallel information transmission, while NLE represents the inverse of the shortest average path length within a node's local subgraph, serving as an indicator of network robustness [50].

Because AUC provides a threshold-independent summary across sparsity values and is sensitive to topological alterations in brain disorders, we calculated the AUC for each network metric [51].

## 2.5. Statistical Analysis

All statistical analyses of demographic variables were conducted using SPSS version 27.0 (IBM Corp., Armonk, NY). Specifically, all comparisons were performed separately at each site: two-sample *t*-tests were used to assess group differences in age, while sex distributions were compared using the chi-square ($\chi^2$) test. Statistical significance was determined using a threshold of $p < 0.05$.

To examine group differences in functional brain networks and associated global and nodal topological metrics between the ASD and HCs, we conducted two-sample *t*-tests using the GRETNA toolbox [47]. We entailed a mega-analysis, which integrates data from multiple sites into a single statistical analysis [52–55], to correct site bias. Specifically, the site was included as a nuisance covariate (using dummy coding for each scanning center) in the statistical model to account for non-biological variance [56]. Statistical significance was determined using false discovery rate (FDR) correction ($p < 0.05$) to control for multiple comparisons across all network properties [57].

To examine the relationship between brain network features and verbal abilities, we performed Pearson correlation analyses in MATLAB (version 2022a). Specifically, for each subject we extracted (1) the *z*-values of those FC edges showing group differences between ASD and HCs, and (2) global and nodal graph-theoretical network metrics. To ensure consistent handling of site effects, associations between VIQ and network features were assessed using a multiple linear regression framework. Specifically, site was included in the model as a dummy-coded nuisance covariate to regress out site-related variance, thereby isolating the specific relationship between VIQ and brain network measures. Pearson correlation coefficients (r) were calculated to evaluate the relationship between network metrics and VIQ scores, with significance set at $p < 0.05$.

## 2.6. Manual Feature Selection

To investigate the impact of feature selection on classification performance, we constructed three 541 × N feature matrices (where rows correspond to participants and columns to features). Following a filter-based feature selection strategy, which is independent of classifier construction [58], we utilized group-level statistical tests to identify features with high discretionary power [59,60]. The raw feature matrix was formed by flattening the upper-triangular entries of each participant's FC matrix into a row vector and concatenating this with the flattened row vector of all computed network metrics. The differential feature matrix was then derived by repeating this procedure across the pooled dataset only for those FC edges and network metrics that showed significant group differences (FDR, $p < 0.05$). While we acknowledge that performing feature selection on the whole dataset can be an issue in some classification contexts [61], this approach was chosen to ensure the selected markers were biologically anchored across the multi-site cohort. Finally, the differential-verbal-ability feature matrix was created by appending each participant's VIQ score as an additional column to the differential feature matrix. For all three matrices, a final column of class labels was added (ASD = 1, HCs = 2) before feeding into a classifier with uniform parameter settings.

### 2.7. Machine Learning

All imaging-derived features were first split into training and holdout test sets by stratified sampling to preserve class proportions, with 80% of the data used for training and 20% reserved for final evaluation. The data partitioning was stratified by class labels only; site was not used as a stratification factor, such that each split contained participants from multiple sites. Within the training set, we performed ten-fold cross-validation: the training data were randomly shuffled and partitioned into ten equal folds, each maintaining the original distribution of classes. In each fold, all preprocessing steps were nested within the fold-specific training data only. Specifically, the Min-Max scaler was fit on the training features and applied to the corresponding validation and test subsets independently into the [1] interval. In each fold, two parallel pipelines were executed. In the first pipeline, a support vector machine classifier with a radial basis function kernel was trained directly on the normalized features using fixed hyperparameters determined in preliminary experiments. In the second pipeline, optional PCA was likewise fit only on the fold-specific training subset, with the decision to use PCA and the proportion of variance to retain treated as parameters to be optimized; the resulting transformation was then applied to the validation subset, followed by UMAP embedding, where the number of neighbors, minimum distance, distance metric, and target dimensionality were likewise tuned within the training fold. The low-dimensional representations were then fed into the same support vector machine classifier with an RBF kernel as used in the first pipeline. Model selection in both pipelines involved grid search over kernel types and regularization parameters (C and γ), class weights were adjusted to compensate for imbalance, probabilistic outputs were enabled, and all randomization steps were governed by a single seed to ensure full reproducibility. After cross-validation, each pipeline's optimal parameter set was used to retrain a final model on the entire training set, and the discriminative performance of these models was assessed on the hold-out test set by computing the AUC.

## 3. Results

### 3.1. Demographic and Clinical Information

The demographic information of the current study was summarized in **Table 1**. A total of 2,168 participants were initially included from the ABIDE I and ABIDE II datasets. Following the application of these criteria, 14 individuals were excluded for missing functional images, 16 for missing structural images, 213 due to poor normalization quality, and 228 due to excessive head motion. A further 55 participants were excluded from sites that did not include both groups. This resulted in an intermediate pool of 1,642 individuals meeting the basic fMRI requirements. From this pool, we further restricted our analysis to participants with available and valid VIQ scores. This yielded a final sample of 541 participants, comprising 219 individuals with ASD and 322 HCs from 12 sites.

**Table 1.** Demographic information of ASD patients and HCs.

| Site Name | Participants | | Sex | | | Age (Years) | | | VIQ Scores | | |
|---|---|---|---|---|---|---|---|---|---|---|---|
| | ASD | HCs | ASD | HCs | *p*-Value | Mean (SD) | | *p*-Value | Mean (SD) | | *p*-Value |
| | | | M/F | M/F | | ASD | HCs | | ASD | HCs | |
| Caltech | 3 | 10 | 3/0 | 6/4 | 0.220 | 25.67 (9.81) | 27.7 (12.20) | 0.798 | 109.33 (9.61) | 112.70 (15.81) | 0.738 |
| ETH | 6 | 19 | 6/0 | 19/0 | - | 20.67 (4.27) | 22.95 (4.78) | 0.308 | 110.00 (14.41) | 114.53 (15.52) | 0.533 |
| GU | 15 | 31 | 14/1 | 15/16 | 0.002 | 10.53 (1.30) | 10.06 (1.88) | 0.390 | 118.53 (12.37) | 119.48 (16.12) | 0.842 |
| NYU1 | 59 | 97 | 48/11 | 77/20 | 0.766 | 14.88 (7.85) | 14.62 (6.40) | 0.820 | 107.03 (17.21) | 114.32 (13.37) | 0.003 |
| Pitt | 22 | 23 | 19/3 | 20/3 | 0.955 | 18.41 (7.14) | 18.96 (6.66) | 0.791 | 106.91 (13.81) | 107.09 (10.31) | 0.961 |
| SDSU | 12 | 21 | 12/0 | 16/5 | 0.070 | 14.58 (1.73) | 13.90 (1.51) | 0.248 | 113.42 (17.75) | 106.10 (10.31) | 0.142 |
| Stanford_1 | 17 | 16 | 14/3 | 12/4 | 0.619 | 9.36 (1.58) | 9.63 (1.70) | 0.638 | 109.59 (21.30) | 111.62 (20.54) | 0.782 |
| Stanford_2 | 17 | 18 | 16/1 | 16/2 | 0.594 | 10.47 (1.23) | 10.50 (1.38) | 0.948 | 110.41 (16.02) | 115.78 (16.21) | 0.332 |
| Trinity2 | 13 | 18 | 13/0 | 18/0 | - | 13.85 (3.58) | 15.94 (2.73) | 0.074 | 115.08 (10.86) | 119.33 (14.32) | 0.376 |
| UCLA | 13 | 38 | 12/1 | 31/7 | 0.369 | 12.38 (1.85) | 12.24 (2.12) | 0.824 | 100.54 (14.66) | 111.11 (10.51) | 0.007 |
| UM | 3 | 4 | 3/0 | 4/0 | - | 15.33 (0.58) | 22.00 (5.83) | 0.112 | 107.67 (11.06) | 112.00 (11.40) | 0.636 |
| USM | 39 | 27 | 39/0 | 27/0 | - | 22.87 (8.43) | 20.78 (6.62) | 0.284 | 97.54 (17.89) | 114.22 (13.12) | <0.001 |

Note: The CMU_1 and CMU_2 sites were excluded due to poor normalization, whereas sites NYU_2 were excluded due to the lack of HCs. ASD, autism spectrum disorder; HCs, healthy controls; VIQ, verbal intelligence quotient; SD, Standard Deviation; M, Male; F, Female; Caltech, California Institute of Technology; ETH, Swiss Federal Institute of Technology Zürich; GU, Georgetown University; NYU1, New York University (Site 1); Pitt, University of Pittsburgh; SDSU, San Diego State University; Stanford_1, Stanford University (Site 1); Stanford_2, Stanford University (Site 2); Trinity2, Trinity College Dublin (Site 2); UCLA, University of California, Los Angeles; UM, University of Michigan; USM, University of Utah School of Medicine.

Group comparisons across sites revealed no significant differences in age or sex distribution between ASD and HCs at most sites ($p > 0.05$), except for the site of Georgetown University (GU) with 14 males and 1 female in the

ASD group versus 15 males and 16 females in the HCs ($p$ = 0.002). As anticipated, VIQ scores were generally lower in ASD, reaching statistical significance at New York University Site 1 (NYU1; $p$ = 0.003), University of California, Los Angeles (UCLA; $p$ = 0.007), and University of Utah School of Medicine (USM; $p$ < 0.001). Finally, to further account for residual between-site variability, all statistical imaging analyses were performed within a mega-analytic regression framework with site entered as a dummy-coded nuisance covariate. Demographic comparisons were conducted separately within each site and are reported descriptively.

## 3.2. Results of FC

Following the computation of FC, group-level comparisons revealed significant alterations in the inter-network connectivity between specific brain regions, as illustrated in **Figure 1**.

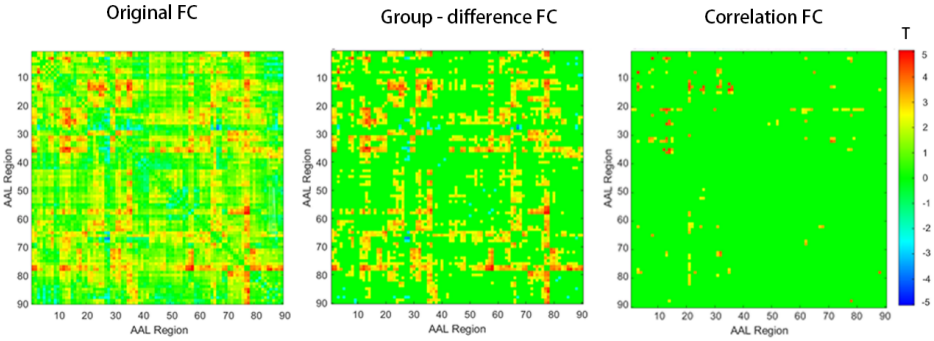


**Figure 1.** *T*-value heatmaps illustrating the progressive refinement of FC features, categorized into the Original FC, Group-difference FC, and Correlation FC matrices.

The Group-difference FC matrix highlights connections that significantly differed between ASD and HCs, as identified by two-sample *t*-tests with FDR correction ($p$ < 0.05). The Correlation FC matrix further refines these group-differentiated connections by retaining only those that were significantly correlated with VIQ scores ($p$ < 0.05), thus emphasizing connections that were both diagnosis-sensitive and cognitively relevant. ASD exhibited widespread increased FC in the DMN, DAN, and FPN ($p$ < 0.05). Conversely, decreased FC was observed within the DMN, limbic, SMN, and VN, and between the FPN and DMN, FPN and limbic, DMN and limbic, VN and SMN, and VAN and DAN ($p$ < 0.05). Correlation analysis identified positive correlations between VIQ scores and FC values involving regions within the FPN and DMN ($p$ < 0.05).

## 3.3. Global Properties of the Functional Brain Networks

As shown in **Figure 2**, both the ASD and HCs demonstrated functional networks with small-world properties across the defined sparsity range (0.05–0.5), as evidenced by AUC values for $\sigma > 1$, $\gamma > 1$, and $\lambda \approx 1$. The AUC of $\gamma$ in the ASD group was significantly lower than that in the HCs ($p$ < 0.05), indicating reduced local clustering in ASD. However, no significant differences were found in the AUCs of $\lambda$, $\sigma$, Cp, or Lp (all $p$ > 0.05), suggesting comparable global integration and small-world topology between groups. Likewise, the AUCs of both Eloc and Eglob did not differ significantly between ASD and HCs ($p$ > 0.05).

## 3.4. Nodal Properties of Functional Brain Networks

As shown in **Figure 3** and **Table 2**, several brain regions exhibited significant alterations in DC and NE in ASD patients relative to HCs.

Specifically, ASD patients demonstrated increased DC and NE in the right opercular inferior frontal gyrus (IFGoperc.R), left triangular inferior frontal gyrus (IFGtriang.L), right triangular inferior frontal gyrus (IFGtriang.R), left medial superior frontal gyrus (SFGmed.L), right anterior cingulate gyrus (ACG.R), left anterior cingulate gyrus (ACG.L), left thalamus (THA.L), and right thalamus (THA.R) ($p$ < 0.05).

Conversely, compared with HCs, DC was lower in ASD patients in the left superior frontal orbital gyrus (ORBsup.L), left rectus gyrus (REC.L), right rectus gyrus (REC.R), and left fusiform gyrus (FUS.L). Decreased NE was also found in ORBsup.L, left orbital middle frontal gyrus (ORBmid.L), REC.L, REC.R, left parahippocampal gyrus (PHG.L),

PHG.R, left amygdala (AMYG.L), right superior occipital gyrus (SOG.R), FUS.L, left superior parietal gyrus (SPG.L), right superior temporal pole (TPSup.R), right middle temporal gyrus (MTG.R), left middle temporal pole (TPMid.L), right middle temporal pole (TPMid.R), left inferior temporal gyrus (ITG.L), and right inferior temporal gyrus (ITG.R) ($p < 0.05$).

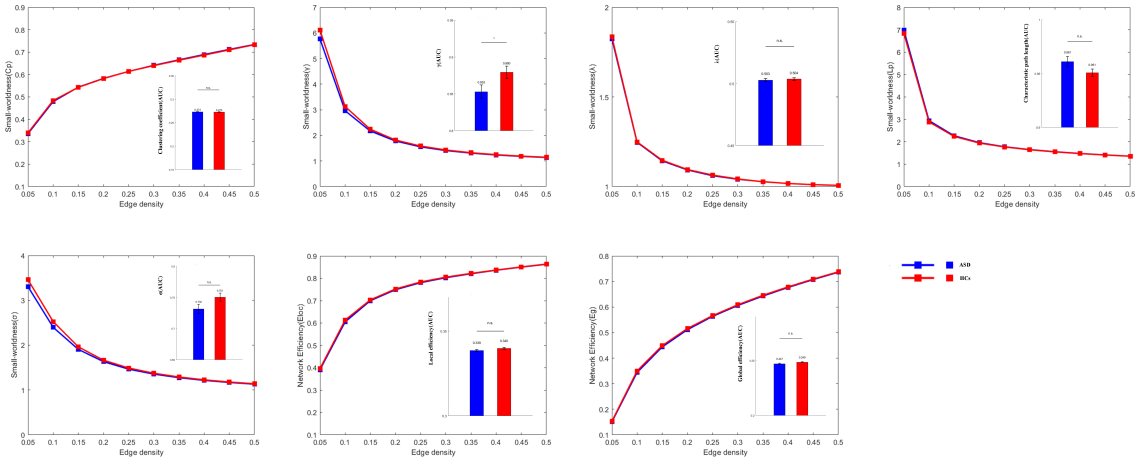

**Figure 2.** Small-world properties and network efficiency of functional brain networks in ASD and HCs.

Note: Functional brain network metrics for individuals with ASD (shown in blue) and HCs (shown in red). The x-axis of the line charts represents the sparsity range (0.05–0.5), and the lines indicate group-averaged values across this range. The bar charts display the AUC for each metric. * indicates significant group differences ($p < 0.05$, two-sample *t*-test, FDR corrected); n.s. denotes non-significant differences. HCs: healthy controls; ASD: autism spectrum disorder; AUC: the area under the receiver operating characteristic curve.

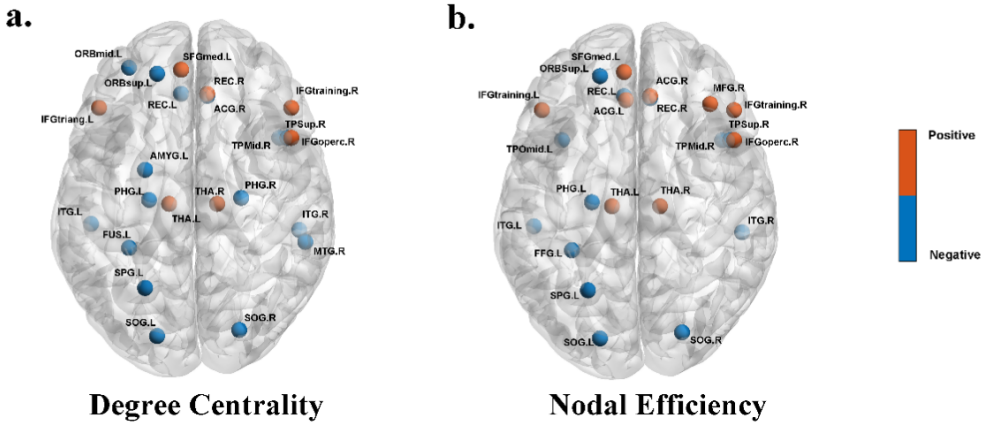


**Figure 3.** Brain regions with significant differences in the (**a**) DC, and (**b**) NE between ASD and HCs.

Note: The red sphere demonstrated that nodal network properties in the ASD group were increased compared with the HCs ($p < 0.05$, FDR corrected). IFGoperc, inferior frontal gyrus, opercular part; IFGtriang, inferior frontal gyrus, triangular part; SFGmed, superior frontal gyrus, medial part; ACG, anterior cingulate gyrus; THA, thalamus; ORBsup, superior frontal gyrus, orbital part; ORBmid, middle frontal gyrus, orbital part; REC, rectus gyrus; PHG, parahippocampal gyrus; AMYG, amygdala; SOG, superior occipital gyrus; FUS, fusiform gyrus; SPG, superior parietal gyrus; TPSup, superior temporal pole; MTG, middle temporal gyrus; TPMid, middle temporal pole; ITG, inferior temporal gyrus.

**Table 2.** The significant differences in node properties between the ASD and HCs.

| Brain Regions | Degree Centrality | | Nodal Efficiency | |
|---|---|---|---|---|
| | *t* Values | *p*-Values | *t* Values | *p*-Values |
| **ASD > HCs** | | | | |
| IFGoperc.R | 2.2781 | 0.0231 | 2.1879 | 0.0291 |
| IFGtriang.L | 3.4769 | 0.0005 | 2.8878 | 0.0040 |
| IFGtriang.R | 2.3763 | 0.0178 | 2.1499 | 0.0320 |
| SFGmed.L | 2.6326 | 0.0087 | 2.1526 | 0.0317 |
| ACG.R | 3.2893 | 0.0011 | 2.7316 | 0.0065 |
| ACG.L | 2.1284 | 0.0338 | n.s. | n.s. |
| THA.L | 3.8845 | 0.0001 | 3.8447 | 0.0001 |
| THA.R | 4.4033 | <0.0001 | 4.2941 | <0.0001 |

**Table 2.** *Cont.*

| Brain Regions | Degree Centrality | | Nodal Efficiency | |
|---|---|---|---|---|
| | *t* Values | *p*-Values | *t* Values | *p*-Values |
| **ASD < HCs** | | | | |
| ORBsup.L | −2.3820 | 0.0176 | −2.4016 | 0.0166 |
| ORBmid.L | n.s. | n.s. | −2.3932 | 0.0170 |
| REC.L | −2.6679 | 0.0078 | −3.1486 | 0.0017 |
| REC.R | −3.3828 | 0.0007 | −3.5156 | 0.0004 |
| PHG.L | −2.2999 | 0.0218 | −2.8396 | 0.0046 |
| PHG.R | n.s. | n.s. | −2.0941 | 0.0367 |
| AMYG.L | n.s. | n.s. | −2.0796 | 0.0380 |
| SOG.L | −1.9341 | 0.0536 | −1.9500 | 0.0516 |
| SOG.R | −2.0096 | 0.0449 | −2.2903 | 0.0223 |
| FUS.L | −3.5071 | 0.0004 | −3.9215 | <0.0001 |
| SPG.L | −1.9278 | 0.0543 | −2.0624 | 0.0396 |
| TPSup.R | −2.1063 | 0.0356 | −2.3226 | 0.0205 |
| MTG.R | n.s. | n.s. | −2.1945 | 0.0286 |
| TPMid.L | −2.0562 | 0.0402 | n.s. | n.s. |
| TPMid.R | −2.8616 | 0.0043 | −2.4384 | 0.0150 |
| ITG.L | −1.9736 | 0.0489 | −2.2616 | 0.0241 |
| ITG.R | −2.4471 | 0.0147 | −2.5677 | 0.0105 |

Note: n.s. denotes non-significant differences; IFGoperc, inferior frontal gyrus, opercular part; IFGtriang, inferior frontal gyrus, triangular part; SFGmed, superior frontal gyrus, medial part; ACG, anterior cingulate gyrus; THA, thalamus; ORBsup, superior frontal gyrus, orbital part; ORBmid, middle frontal gyrus, orbital part; REC, rectus gyrus; PHG, parahippocampal gyrus; AMYG, amygdala; SOG, superior occipital gyrus; FUS, fusiform gyrus; SPG, superior parietal gyrus; TPSup, superior temporal pole; MTG, middle temporal gyrus; TPMid, middle temporal pole; ITG, inferior temporal gyrus.

## 3.5. Correlation between Network Metrics and VIQ Scores

The correlations between VIQ scores and the topological attributes of five key nodes were presented in **Figure 4**. DC of the bilateral ACG was negatively correlated with VIQ (left ACG: r = -0.085, $p$ = 0.049; right ACG: r = -0.098, $p$ = 0.023). In contrast, VIQ scores were positively correlated with DC of the left SOG (r = 0.107, $p$ = 0.013) and with NE of the bilateral SOG (left SOG: r = 0.119, $p$ = 0.005; right SOG: r = 0.083, $p$ = 0.053). No other graph-theoretical metrics or brain regions showed significant associations with VIQ. Moreover, after correlating FC with VIQ scores, several network pairs exhibited significant negative associations, including connections between the FPN and DMN; FPN and limbic networks; DMN and limbic networks; VN and SMN networks; and DAN and VAN.

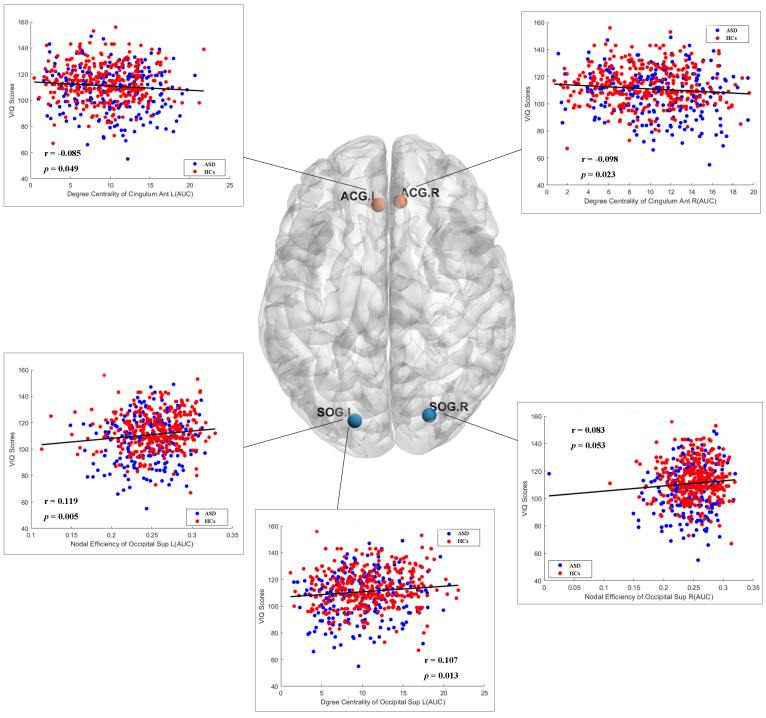


**Figure 4.** Scatter plots of node attributes versus VIQ scores for both ASD (blue) and HCs (red) groups.
Note: ACG, anterior cingulate gyrus; SOG, superior occipital gyrus; L, left; R, right; VIQ, verbal intelligence quotient.

### 3.6. Classification Accuracy

A summary of classification performance for each feature set and model is presented in **Table 3**. When using a standard SVM classifier without dimensionality reduction, manual feature selection based on group differences increased the AUC from 0.7143 (Raw feature set) to 0.7336. Incorporating VIQ scores into the group-difference features further raised the AUC to 0.7451.

**Table 3.** Area under the receiver operating characteristic curve of feature sets and models.

| Feature Matrices | SVM | PCA_UMAP_SVM |
|---|---|---|
| Raw Features | 0.7143 | 0.7514 |
| Group-difference Features | 0.7336 | 0.7024 |
| Group-difference_VIQ Features | 0.7451 | 0.7217 |

Note: SVM, support vector machine; PCA, principal component analysis; UMAP, uniform manifold approximation and projection; VIQ, verbal intelligence quotient.

When PCA was applied followed by UMAP before SVM classification, the highest AUC (0.7514) was obtained using the Raw feature set. Applying PCA and UMAP to the group-difference features yielded an AUC of 0.7024, and applying PCA and UMAP to the group-difference + VIQ features yielded an AUC of 0.7217. Manifold-based dimensionality reduction on the full feature matrix achieved the best performance, while including VIQ information still improved classification within the group-difference features.

## 4. Discussion

In the present study, we examined brain functional alterations associated with verbal cognitive functioning in ASD using FC and network topology and VIQ scale, and also evaluated classification performance using SVM and UMAP manifold learning. There were three main results: (1) ASD patients showed widespread FC alterations, with decreased inter-network connectivity among several large-scale networks and increased intra-network connectivity in regions involved in social and sensory processing; (2) Correlation analyses of network metrics revealed significant changes of DC and NE in verbal-ability-related regions; (3) Conventional SVM required manual feature selection to achieve competitive accuracy, whereas SVM with manifold learning-based dimensionality reduction achieved superior performance using raw features without manual selection. Moreover, incorporating VIQ scores improved classification accuracy, suggesting that VIQ-related network features capture both verbal ability alterations in ASD, providing a proof-of-principle for integrating behavioral scales into neuroimaging analysis.

The FC results revealed reduced connectivity within the DMN, limbic, and sensory-motor systems, together with increased inter-network FC across large-scale networks in ASD. While Just et al. [62] reported reduced long-range connectivity in ASD using task-based fMRI during language processing, our findings extend this framework by demonstrating that increased FC and reduced network segregation can coexist with selective long-range connectivity reductions during the resting state. This topological misalignment provides strong empirical support for the "multiple-network" view of ASD [63] and is theoretically rooted in the excitation/inhibition (E/I) imbalance model [64]. Specifically, an elevated E/I ratio—potentially stemming from diminished GABAergic inhibitory signaling—may lead to excessive local "neural noise" [65], manifesting as the observed over-integration and compensatory sensory scaffolding in perceptual-motor networks [2]. Moreover, our findings demonstrated increased local connectivity within the DMN regions as well as within the VN and SMN resting-state networks, consistent with previous reports [66,67]. However, unlike Yerys et al. [67], who reported decreased connectivity between DMN ROIs and regions within primary sensory, FPN, subcortical, and reward networks, our study found reduced connectivity primarily within the DMN, limbic, SMN, and VN, as well as between FPN-DMN, FPN-limbic, DMN-limbic, VN-SMN, and VAN-DAN. This discrepancy may be due to our larger sample size, indicating that the patterns of hypoconnectivity in ASD might be more localized and network-specific than previously reported. Collectively, these FC results underscore the emerging view that ASD is characterized not by uniform hypo- or hyperconnectivity but by a misalignment of network segregation and integration associated with individual differences in verbal ability.

Graph-theoretical analysis of global network topology demonstrated that both ASD and HCs maintained small-world characteristics ($\sigma > 1$, $\gamma > 1$, $\lambda \approx 1$) across a sparsity range of 0.05–0.5. Specifically, the ASD group exhibited a significant reduction in the normalized $\gamma$ AUC, indicating a loss of local modularity. These findings align with the the-

oretical model of optimal segregation-integration balance described by Bullmore and Sporns [68] and Rubinov and Sporns [46], in which disruption to γ compromises modular processing, prompting—but failing to fully realize—compensatory global interactions. In contrast, although the characteristic Lp AUC showed an increase in the ASD group, these differences did not reach statistical significance after correction. Moreover, the AUC values for Eloc, λ, Eglob, and σ were all lower in the ASD group, but these differences did not reach significance, further implying a subtle decline in overall network integration. Consistent with our results, prior studies [12,69] have similarly reported declines in σ alongside increases in Lp, suggesting a potential trend toward altered small-world topology in ASD, though our data indicates that local clustering deficits γ emerge as the most robust global network aberration in this multisite sample. Although multiple small-world related metrics showed numerically consistent deviations, only γ survived correction for multiple comparisons, indicating that evidence for widespread small-world disruption is weak in this multisite sample. Instead, the results highlight γ as a potentially sensitive indicator of altered modular organization in ASD.

At the nodal level, ASD showed a distinct imbalance between hyper- and hypo-connectivity across regions subserving language production, semantic integration, and socio-emotional processing. DC and NE were significantly elevated in bilateral IFGtriang, IFGoperc, SFGmed, ACG, and THA. These regions form part of the executive-language control network and are critical for top-down regulation of speech production, syntactic processing, and attentional modulation [70,71]. Compared to HCs, ASD participants exhibited significantly increased DC in the IFG, ACG, and thalamus, consistent with previous findings of elevated DC in these regions in ASD [6], suggesting that hyper-centrality within frontal and limbic circuits may underlie atypical cognitive and affective processing in ASD. In contrast, we also observed decreased DC in temporal regions, including the MTG, ITG, and temporal pole, whereas Lee et al. reported more widespread DC increases across the STG. This difference may reflect their age-stratified approach versus our lifespan sample, indicating that hypoconnectivity in temporal regions may vary with age or individual heterogeneity. Additionally, regions implicated in semantic memory (PHG), emotion regulation (AMYG, REC), and VN recognition (FUS, SOG), along with the orbitofrontal cortex (ORBsup, ORBmid), exhibited reduced centrality and efficiency—echoing previous reports of disrupted fusiform-amygdala coupling in ASD [72]. These alterations likely impeded integration of emotional and contextual information during language use [2], consistent with documented deficits in pragmatic language and context-dependent communication in ASD [73]. Taken together, the nodal architecture suggests that ASD is characterized by frontally weighted hyperconnectivity compensating for weakened posterior-limbic integration. This imbalance may help explain why individuals with ASD, despite preserved or even enhanced integration in control-related regions, struggle to ground language in contextually and socially appropriate ways—supporting our hypothesis that altered nodal connectivity underlies the heterogeneous verbal ability profiles observed in ASD.

Correlation analyses revealed that decreased FC between the FPN, DMN, and limbic networks was negatively associated with VIQ, consistent with Redcay et al. [74], who reported that lower DMN connectivity correlated with greater communication difficulties in ASD. At the nodal level, DC of the bilateral ACG was negatively associated with VIQ, whereas DC and NE of the SOG were positively correlated with VIQ. The negative ACG–VIQ association may reflect inefficient neural recruitment [75], such that a hyper-central ACG serves as a non-specialized, domain-general hub that is recruited excessively during verbal processing, potentially reducing processing efficiency and increasing neural noise [76]. This interpretation is consistent with the role of the ACG in attentional control and conflict monitoring, as described by Bush et al. [77], and aligns with the broader notion that ASD may involve less efficient allocation of cognitive resources across large-scale networks [78]. In contrast, enhanced SOG connectivity appears to support visual-based scaffolding of verbal processes, corroborating Vulchanova et al.'s [2] notion of augmented reliance on contextual visual cues. However, these findings should be viewed as preliminary, particularly given that the SOG-related association only reached marginal significance ($p = 0.053$). Nevertheless, these suggestive associations align with Johnson et al.'s [15] assertion that VIQ reflects underlying network integrity and highlight the potential of combining neurofunctional and psychometric measures to capture the cognitive heterogeneity of ASD. Although statistically significant, the small magnitude of these correlations suggests that VIQ is associated with a modest, yet potentially meaningful, portion of the variance in the nodal properties of these regions. No other nodal or global metrics show significant VIQ correlations, indicating that ACG and SOG serve as principal neural substrates linking network topology to verbal ability.

For the ML results, the PCA + UMAP approach on raw features achieved the highest overall AUC of approximately 0.7514. In parallel, using SVM with the selected differential features combined with VIQ also reached a comparable AUC of 0.7451. These AUC values are broadly in line with existing ABIDE classification studies, suggesting that the classifier captures meaningful patterns, while primarily as a proof-of-principle analysis. The superior performance of the PCA + UMAP pipeline on raw features may indicate that manifold learning is better suited to high-dimensional neuroimaging data, in which class information is distributed across many weak, interacting signals rather than concentrated in a small number of individually salient features. In this high-dimensional space, UMAP may uncover latent structural patterns that manual selection cannot capture. Conversely, the manual-selection pipeline benefited most significantly from the incorporation of VIQ. This suggests that the discriminative power of behavioral indices like VIQ is most effectively leveraged when the feature space is already constrained and biologically grounded. Within the standard SVM pipeline, adding VIQ to the group-difference features improved classification performance. Under the PCA_UMAP_SVM pipeline, VIQ also improved the group-difference feature set, but the raw feature set still achieved the best overall AUC. These results reinforce Pereira et al.'s [19] demonstration of SVM's sensitivity to high-dimensional neuroimaging features and extend Casanova et al.'s [25] finding that manifold learning uncovers intrinsic data structure to enhance classification. The consistent performance gain from integrating VIQ underscores Lin et al.'s [5] call for multimodal biomarkers. Overall, our ML analysis illustrates that low-dimensional embeddings, combined with behavioral indices, constitute a useful analytical strategy for exploring ASD phenotype stratification.

Despite these findings, this study has several limitations. The cross-sectional design limited our ability to characterize longitudinal changes in network topology and verbal functioning, and future studies with follow-up assessments are needed to clarify causal relationships and developmental trajectories. Although the multisite sample increased statistical power, heterogeneity in scanner hardware, acquisition parameters, and recruitment strategies may have introduced additional noise. Additionally, because our brain-behavior correlation analyses were conducted across the pooled sample of both ASD and HC individuals, these correlations must be interpreted cautiously, as they might reflect a combination of diagnosis-related separation and VIQ-related variation rather than purely within-ASD neural correlates. While we addressed site-related heterogeneity by including site as a dummy-coded nuisance covariate in all regression models. Because the demographic distributions were broadly comparable at the group level and several sites had small sample sizes, no additional covariates were entered in the current models. Future work may further improve control of non-specific factors by more closely matching participants on demographic characteristics. Furthermore, the machine-learning validation framework was not explicitly site-aware, and since feature selection was performed on the full dataset prior to model training and cross-validation, this procedure may have introduced some degree of feature-selection leakage, potentially yielding somewhat optimistic classification performance estimates. Given the heterogeneous nature of the ABIDE dataset, future studies should implement site-independent validation to further confirm the clinical transportability of these VIQ-anchored biomarkers. Finally, although UMAP-based dimensionality reduction modestly improved classification performance, the resulting low-dimensional embeddings lack direct neurobiological interpretability, warranting more transparent modeling and feature-level analyses in future studies.

## 5. Conclusions

In summary, individuals with ASD exhibited dysregulated functional connections across multiple brain networks and regions, and these alterations showed associations with VIQ. Our findings demonstrate that the automated PCA + UMAP pipeline applied to the Raw feature set achieved the highest classification performance, while the manually selected feature sets augmented with VIQ also showed modest but competitive discrimination between ASD and HCs, consistent with findings from other large-scale multisite datasets. These results provide a neuroscientific basis for network-level alterations associated with individual differences in verbal ability in ASD and support the relevance of VIQ-related features.

## Author Contributions

X.J., H.M., and J.W. conceived and designed this study. L.C. (Lulu Cheng), L.Z. and Z.H. compiled the ABIDE database. J.W. executed the data analysis and wrote the first manuscript. L.C. (Lanfen Chen), J.S., H.Z. and L.Z. helped

coordinate the study and revised the manuscript. H.M., J.W., and L.C. (Lanfen Chen) contributed equally to this work. All authors have made significant scientific contributions to this article. All authors have read and agreed to the published version of the manuscript.

## Funding

This work was supported by the National Natural Science Foundation of China (grant number 82374578), in collaboration with the First Affiliated Hospital of Tianjin University of Traditional Chinese Medicine, under the project titled "External Manifestations and Internal Mechanisms of 'Effective Qi Arrival' in Tongguan Liqiao Acupuncture," and by the National Social Science Foundation of China (grant number 25CYY083), under the project titled "AI-Empowered Precision Intervention and Dynamic Effect Evaluation for Pragmatic Impairment in Children with Autism," and by the Open Project of the Heilongjiang Provincial Key Laboratory of Autonomous Intelligence and Information Processing (Project No. ZZXC202303), under the project "Research on Real-Time Target Recognition Methods for UAV Images Based on Deep Reinforcement Learning."

## Institutional Review Board Statement

The study was conducted in accordance with the Declaration of Helsinki and utilized data from the Autism Brain Imaging Data Exchange (ABIDE) consortium. Ethical approval for the original data collection was obtained at each participating site from the respective institutional review boards or ethics committees. For the present secondary analysis of publicly available, anonymized data, additional ethical approval was waived.

## Informed Consent Statement

Patient consent was waived due to the use of publicly available anonymized data from the ABIDE consortium.

## Data Availability Statement

The data used in this study were obtained from the Autism Brain Imaging Data Exchange (http://fcon_1000.projects.nitrc.org/indi/abide/) public database.

## Acknowledgments

We thank the Hangzhou NaoHai Technology Laboratory (https://www.brainimaging.cn) for the technical support provided by its scientific research platform in this study.

## Conflicts of Interest

The authors declare that this research has no financial conflicts of interest.

## AI Use Statement

During the preparation of this work, the authors used ChatGPT (OpenAI) for language editing and manuscript wording refinement. The authors subsequently reviewed and edited the content as necessary and take full responsibility for the final content of the published article.

## References

1. American Psychiatric Association. *Diagnostic and Statistical Manual of Mental Disorders: DSM-5*; American Psychiatric Association: Washington, DC, USA, 2013.
2. Vulchanova, M.; Saldaña, D.; et al. Figurative language processing in atypical populations: The ASD perspective. *Front. Hum. Neurosci.* **2015**, *9*, 24. [CrossRef]
3. Dichter, G.S. Functional magnetic resonance imaging of autism spectrum disorders. *Dialogues Clin. Neurosci.* **2012**, *14*, 319–351. [CrossRef]
4. Biswal, B.B.; Uddin, L.Q. The history and future of resting-state functional magnetic resonance imaging. *Nature* **2025**, *641*, 1121–1131. [CrossRef]
5. Lin, Q.; Shi, Y.; Huang, H.; et al. Functional brain network alterations in the co-occurrence of autism spec-

trum disorder and attention deficit hyperactivity disorder. *Eur. Child Adolesc. Psychiatry* **2024**, *33*, 369–380. [CrossRef]
6. Lee, Y.; Park, B.Y.; James, O.; et al. Autism spectrum disorder related functional connectivity changes in the language network in children, adolescents and adults. *Front. Hum. Neurosci.* **2017**, *11*, 418. [CrossRef]
7. Márquez-García, A.V.; Vakorin, V.A.; Kozhemiako, N.; et al. Atypical Brain Connectivity During Pragmatic and Semantic Language Processing in Children with Autism. *Brain Sci.* **2024**, *14*, 1066. [CrossRef]
8. Schaeffer, J.; Abd El-Raziq, M.; Castroviejo, E.; et al. Language in autism: Domains, profiles and co-occurring conditions. *J. Neural Transm.* **2023**, *130*, 433–457. [CrossRef]
9. Alamdari, S.B.; Sadeghi Damavandi, M.; Zarei, M.; et al. Cognitive theories of autism based on the interactions between brain functional networks. *Front. Hum. Neurosci.* **2022**, *16*, 828985. [CrossRef]
10. Horien, C.; Floris, D.L.; Greene, A.S.; et al. Functional connectome-based predictive modeling in autism. *Biol. Psychiatry* **2022**, *92*, 626–642. [CrossRef]
11. Rudie, J.D.; Brown, J.A.; Beck-Pancer, D.; et al. Altered functional and structural brain network organization in autism. *Neuroimage-Clin.* **2012**, *2*, 79–94. [CrossRef]
12. Keown, C.L.; Datko, M.C.; Chen, C.P.; et al. Network organization is globally atypical in autism: A graph theory study of intrinsic functional connectivity. *Biol. Psychiatry-Cogn. Neurosci. Neuroimaging* **2017**, *2*, 66–75. [CrossRef]
13. Chen, L.; Chen, Y.; Zheng, H.; et al. Changes in the topological organization of the default mode network in autism spectrum disorder. *Brain Imaging Behav.* **2021**, *15*, 1058–1067. [CrossRef]
14. Moraglia, L.E.; Weigman, B.; Abdi, H.; et al. Brain morphometry in infants later diagnosed with autism is related to later language skills. *Hum. Brain Mapp.* **2025**, *46*, e70221. [CrossRef]
15. Johnson, C.N.; Ramphal, B.; Koe, E.; et al. Cognitive correlates of autism spectrum disorder symptoms. *Autism Res.* **2021**, *14*, 2405–2411. [CrossRef]
16. Klöppel, S.; Abdulkadir, A.; Jack, C.R.; et al. Diagnostic neuroimaging across diseases. *Neuroimage* **2012**, *61*, 457–463. [CrossRef]
17. Orrù, G.; Pettersson-Yeo, W.; Marquand, A.F.; et al. Using support vector machine to identify imaging biomarkers of neurological and psychiatric disease: A critical review. *Neurosci. Biobehav. Rev.* **2012**, *36*, 1140–1152. [CrossRef]
18. Ahsan, M.M.; Luna, S.A.; Siddique, Z. Machine-learning-based disease diagnosis: A comprehensive review. *Healthcare* **2022**, *10*, 541. [CrossRef]
19. Pereira, F.; Mitchell, T.; Botvinick, M. Machine learning classifiers and fMRI: A tutorial overview. *Neuroimage* **2009**, *45*, S199–S209. [CrossRef]
20. Bi, X.; Wang, Y.; Shu, Q.; et al. Classification of autism spectrum disorder using random support vector machine cluster. *Front. Genet.* **2018**, *9*, 18. [CrossRef]
21. Ibrahim, B.; Suppiah, S.; Ibrahim, N.; et al. Diagnostic power of resting-state fMRI for detection of network connectivity in Alzheimer's disease and mild cognitive impairment: A systematic review. *Hum. Brain Mapp.* **2021**, *42*, 2941–2968. [CrossRef]
22. Lin, L.; Zhang, J.; Liu, Y.; et al. Aberrant brain functional networks in type 2 diabetes mellitus: A graph theoretical and support-vector machine approach. *Front. Hum. Neurosci.* **2022**, *16*, 974094. [CrossRef]
23. Li, W.; Wang, Z.; Zhang, L.; et al. Remodeling Pearson's correlation for functional brain network estimation and autism spectrum disorder identification. *Front. Neuroinform.* **2017**, *11*, 55. [CrossRef]
24. Thomas, C.G.; Harshman, R.A.; Menon, R.S. Noise reduction in BOLD-based fMRI using component analysis. *Neuroimage* **2002**, *17*, 1521–1537. [CrossRef]
25. Casanova, R.; Lyday, R.G.; Bahrami, M.; et al. Embedding functional brain networks in low dimensional spaces using manifold learning techniques. *Front. Neuroinform.* **2021**, *15*, 740143. [CrossRef]
26. Healy, J.; McInnes, L. Uniform manifold approximation and projection. *Nat. Rev. Methods Prim.* **2024**, *4*, 82. [CrossRef]
27. Bradley, A.P. The use of the area under the ROC curve in the evaluation of machine learning algorithms. *Pattern Recogn.* **1997**, *30*, 1145–1159. [CrossRef]
28. Ling, C.X.; Huang, J.; Zhang, H. AUC: A better measure than accuracy in comparing learning algorithms. In *Advances in Artificial Intelligence*; Xiang, Y., Chaib-draa, B., Eds.; Springer: Berlin, Germany, 2003; pp. 329–341.
29. Fawcett, T. An introduction to ROC analysis. *Pattern Recogn. Lett.* **2006**, *27*, 861–874. [CrossRef]
30. Sun, L.; Wang, J.; Wei, J. AVC: Selecting discriminative features on basis of AUC by maximizing variable complementarity. *BMC Bioinform.* **2017**, *18*, 50. [CrossRef]

31. Saponaro, S.; Lizzi, F.; Serra, G.; et al. Deep learning based joint fusion approach to exploit anatomical and functional brain information in autism spectrum disorders. *Brain Inform.* **2024**, *11*, 2. [CrossRef]
32. Marek, S.; Tervo-Clemmens, B.; Calabro, F.J.; et al. Reproducible brain-wide association studies require thousands of individuals. *Nature* **2022**, *603*, 654–660. [CrossRef]
33. Larson, C.; Rivera-Figueroa, K.; Thomas, H.R.; et al. Structural language impairment in autism spectrum disorder versus loss of autism diagnosis: Behavioral and neural characteristics. *Neuroimage-Clin.* **2022**, *34*, 103043. [CrossRef]
34. Wu, Y.; Lu, C.; Li, M.; et al. Atypical developmental patterns of sensorimotor-related networks in autism spectrum disorder: A BrainAGE study based on resting-state fMRI. *Autism Res.* **2025**, *18*, 765–773. [CrossRef]
35. Di Martino, A.; Yan, C.G.; Li, Q.; et al. The autism brain imaging data exchange: Towards a large-scale evaluation of the intrinsic brain architecture in autism. *Mol. Psychiatry* **2014**, *19*, 659–667. [CrossRef]
36. Di Martino, A.; O'Connor, D.; Chen, B.; et al. Enhancing studies of the connectome in autism using the autism brain imaging data exchange II. *Sci. Data* **2017**, *4*, 170010. [CrossRef]
37. Wechsler, D. *Wechsler Abbreviated Scale of Intelligence*; Psychological Corporation: San Antonio, TX, USA, 1999.
38. Jia, X.-Z.; Wang, J.; Sun, H.-Y.; et al. RESTplus: An improved toolkit for resting-state functional magnetic resonance imaging data processing. *Sci. Bull.* **2019**, *64*, 953–954. [CrossRef]
39. Friston, K.J.; Williams, S.; Howard, R.; et al. Movement-related effects in fMRI time-series. *Magn. Reson. Med.* **1996**, *35*, 346–355. [CrossRef]
40. Tzourio-Mazoyer, N.; Landeau, B.; Papathanassiou, D.; et al. Automated anatomical labeling of activations in SPM using a macroscopic anatomical parcellation of the MNI MRI single-subject brain. *Neuroimage* **2002**, *15*, 273–289. [CrossRef]
41. Dai, Z.; Yan, C.; Wang, Z.; et al. Discriminative analysis of early Alzheimer's disease using multi-modal imaging and multi-level characterization with multi-classifier (M3). *Neuroimage* **2012**, *59*, 2187–2195. [CrossRef]
42. Wee, C.-Y.; Yap, P.-T.; Zhang, D.; et al. Identification of MCI individuals using structural and functional connectivity networks. *Neuroimage* **2012**, *59*, 2045–2056. [CrossRef]
43. Zeng, L.-L.; Shen, H.; Liu, L.; et al. Identifying major depression using whole-brain functional connectivity: A multivariate pattern analysis. *Brain* **2012**, *135*, 1498–1507. [CrossRef]
44. Yeo, B.T.; Krienen, F.M.; Sepulcre, J.; et al. The organization of the human cerebral cortex estimated by intrinsic functional connectivity. *J. Neurophysiol.* **2011**, *106*, 1125–1165. [CrossRef]
45. Schaefer, A.; Kong, R.; Gordon, E.M.; et al. Local-global parcellation of the human cerebral cortex from intrinsic functional connectivity MRI. *Cereb. Cortex* **2018**, *28*, 3095–3114. [CrossRef]
46. Rubinov, M.; Sporns, O. Complex network measures of brain connectivity: Uses and interpretations. *Neuroimage* **2010**, *52*, 1059–1069. [CrossRef]
47. Wang, J.; Wang, X.; Xia, M.; et al. GRETNA: A graph theoretical network analysis toolbox for imaging connectomics. *Front. Hum. Neurosci.* **2015**, *9*, 386. [CrossRef]
48. Watts, D.J.; Strogatz, S.H. Collective dynamics of 'small-world' networks. *Nature* **1998**, *393*, 440–442. [CrossRef]
49. Freeman, L.C. Centrality in social networks conceptual clarification. *Soc. Netw.* **1978**, *1*, 215–239. [CrossRef]
50. Achard, S.; Bullmore, E. Efficiency and cost of economical brain functional networks. *PLOS Comput. Biol.* **2007**, *3*, e17. [CrossRef]
51. Zhang, J.; Wang, J.; Wu, Q.; et al. Disrupted brain connectivity networks in drug-naive, first-episode major depressive disorder. *Biol. Psychiatry* **2011**, *70*, 334–342. [CrossRef]
52. van Rooij, D.; Anagnostou, E.; Arango, C.; et al. Cortical and subcortical brain morphometry differences between patients with autism spectrum disorder and healthy individuals across the lifespan: results from the ENIGMA ASD working group. *Am. J. Psychiatry* **2018**, *175*, 359–369. [CrossRef]
53. Cheng, L.; Zhan, L.; Huang, L.; et al. The atypical functional connectivity of Broca's area at multiple frequency bands in autism spectrum disorder. *Brain Imaging Behav.* **2022**, *16*, 2627–2636. [CrossRef]
54. Onitsuka, T.; Hirano, Y.; Nemoto, K.; et al. Trends in big data analyses by multicenter collaborative translational research in psychiatry. *Psychiatry Clin. Neurosci.* **2022**, *76*, 1–14. [CrossRef]
55. Steele, N.; Huggins, A.A.; Morey, R.A.; et al. Image-based meta- and mega-analysis (IBMMA): A unified framework for large-scale, multi-site, neuroimaging data analysis. *Neuroimage* **2025**, *322*, 121554. [CrossRef]
56. Vieira, S.; Gong, Q.; Scarpazza, C.; et al. Neuroanatomical abnormalities in first-episode psychosis across independent samples: A multi-centre mega-analysis. *Psychol. Med.* **2021**, *51*, 340–350. [CrossRef]
57. Benjamini, Y.; Hochberg, Y. Controlling the false discovery rate: A practical and powerful approach to multiple

testing. *J. R. Stat. Soc. Ser. B Methodol.* **1995**, *57*, 289–300. [CrossRef]
58. Guyon, I.; Elisseeff, A. An introduction to variable and feature selection. *J. Mach. Learn. Res.* **2003**, *3*, 1157–1182.
59. Arbabshirani, M.R.; Kiehl, K.A.; Pearlson, G.D.; et al. Classification of schizophrenia patients based on resting-state functional network connectivity. *Front. Neurosci.* **2013**, *7*, 133. [CrossRef]
60. Dyrba, M.; Grothe, M.; Kirste, T.; et al. Multimodal analysis of functional and structural disconnection in Alzheimer's disease using multiple kernel SVM. *Hum. Brain Mapp.* **2015**, *36*, 2118–2131. [CrossRef]
61. Arbabshirani, M.R.; Plis, S.; Sui, J.; et al. Single subject prediction of brain disorders in neuroimaging: Promises and pitfalls. *Neuroimage* **2017**, *145*, 137–165. [CrossRef]
62. Just, M.A.; Cherkassky, V.L.; Keller, T.A.; et al. Cortical activation and synchronization during sentence comprehension in high-functioning autism: Evidence of underconnectivity. *Brain* **2004**, *127*, 1811–1821. [CrossRef]
63. Uddin, L.Q. Salience processing and insular cortical function and dysfunction. *Nat. Rev. Neurosci.* **2015**, *16*, 55–61. [CrossRef]
64. Rubenstein, J.L.; Merzenich, M.M. Model of autism: Increased ratio of excitation/inhibition in key neural systems. *Genes Brain Behav.* **2003**, *2*, 255–267. [CrossRef]
65. Sohal, V.S.; Rubenstein, J.L.R. Excitation-inhibition balance as a framework for investigating mechanisms in neuropsychiatric disorders. *Mol. Psychiatry* **2019**, *24*, 1248–1257. [CrossRef]
66. Washington, S.D.; Gordon, E.M.; Brar, J.; et al. Dysmaturation of the default mode network in autism. *Hum. Brain Mapp.* **2014**, *35*, 1284–1296. [CrossRef]
67. Yerys, B.E.; Gordon, E.M.; Abrams, D.N.; et al. Default mode network segregation and social deficits in autism spectrum disorder: Evidence from non-medicated children. *Neuroimage-Clin.* **2015**, *9*, 223–232. [CrossRef]
68. Bullmore, E.; Sporns, O. Complex brain networks: Graph theoretical analysis of structural and functional systems. *Nat. Rev. Neurosci.* **2009**, *10*, 186–198. [CrossRef]
69. Peng, L.; Liu, X.; Ma, D.; et al. The altered pattern of the functional connectome related to pathological biomarkers in individuals for autism spectrum disorder identification. *Front. Neurosci.* **2022**, *16*, 913377. [CrossRef]
70. Friederici, A.D. The brain basis of language processing: from structure to function. *Physiol. Rev.* **2011**, *91*, 1357–1392. [CrossRef]
71. Cristia, A.; Seidl, A.; Junge, C.; et al. Predicting individual variation in language from infant speech perception measures. *Child Dev.* **2014**, *85*, 1330–1345. [CrossRef]
72. Kleinhans, N.M.; Richards, T.; Sterling, L.; et al. Abnormal functional connectivity in autism spectrum disorders during face processing. *Brain* **2008**, *131*, 1000–1012. [CrossRef]
73. Márquez-García, A.V.; Ng, B.K.; Iarocci, G.; et al. Atypical associations between functional connectivity during pragmatic and semantic language processing and cognitive abilities in children with autism. *Brain Sci.* **2023**, *13*, 1448. [CrossRef]
74. Redcay, E.; Moran, J.M.; Mavros, P.L.; et al. Intrinsic functional network organization in high-functioning adolescents with autism spectrum disorder. *Front. Hum. Neurosci.* **2013**, *7*, 573. [CrossRef]
75. Minshew, N.J.; Williams, D.L. The new neurobiology of autism: Cortex, connectivity, and neuronal organization. *Arch. Neurol.* **2007**, *64*, 945–950. [CrossRef]
76. Davis, G.; Plaisted-Grant, K. Low endogenous neural noise in autism. *Autism* **2015**, *19*, 351–362. [CrossRef]
77. Bush, G.; Luu, P.; Posner, M.I.; et al. Cognitive and emotional influences in anterior cingulate cortex. *Trends Cogn. Sci.* **2000**, *4*, 215–222. [CrossRef]
78. Kennedy, D.P.; Redcay, E.; Courchesne, E. Failing to deactivate: Resting functional abnormalities in autism. *Proc. Natl. Acad. Sci. USA* **2006**, *103*, 8275–8280. [CrossRef]